Journal of the European Ceramic Society 38 (2018) 1621–1631

Contents lists available at ScienceDirect

Journal of the European Ceramic Society

journal homepage: www.elsevier.com/locate/jeurceramsoc

Original Article

Electrosteric colloidal stabilization for obtaining $SrTiO_3/TiO_2$ heterojunction: Microstructural evolution in the interface and photonics properties

Rafael A.C. Amoresi[a,*], Vinícius Teodoro[b], Guilhermina F. Teixeira[a], Maximo S. Li[c], Alexandre Z. Simões[d], Leinig A. Perazolli[a], Elson Longo[a,b], Maria A. Zaghete[a]

[a] Interdisciplinary Laboratory of Electrochemistry and Ceramics, LIEC – Chemistry Institute, São Paulo State University – UNESP, 14800-060 Araraquara, SP, Brazil
[b] Interdisciplinary Laboratory of Electrochemistry and Ceramics, LIEC – Department of Chemistry, Universidade Federal de São Carlos – UFSCAR, 13565-905 São Carlos, SP, Brazil
[c] Institute of Physics of São Carlos, University of São Paulo – USP, 13560-970, São Carlos, Brazil
[d] Faculty of Engineering of Guaratinguetá, São Paulo State University – UNESP, 12516-410, Guaratinguetá, SP, Brazil

ARTICLE INFO

Keywords:
Heterojunction
Interface
$SrTiO_3/TiO_2$
Photonic

ABSTRACT

Researches on solids heterojunctions has proven to be an important field for technological applications due to synergism achieved by interface phenomena. In this work, we present an understanding of $SrTiO_3/TiO_2$ interface and its effects on structural and microstructural characteristics, and relate them to photoluminescence properties of heterojunctions obtained by a simple method. It was observed that $SrTiO_3$ proportion directly influences the structural order-disorder, as observed by X-Ray diffraction, Raman spectroscopy and Transmission electron microscopy. Photoluminescence behavior of heterojunction with 1% of $SrTiO_3$ showed a shift to blue emission region compared to TiO_2, and enhanced of emission intensity compared to $SrTiO_3$, resulted from defects generated by interface effects, attracting possible applications on selective color emitter. Therefore, we conclude that in same materials phases, nature and concentration of structural defects has strong dependence of $SrTiO_3$ concentration, which leads to different photoluminescence properties.

1. Introduction

In recent years, the search for functional materials has grown due to increasing demand for better electronic device technologies, particularly the optoelectronics devices. Nanocomposite stand out in this field due to the synergistic effect resulting from the junction of two different materials phases promoting its applications in several devices, such as solar cells [1], sensors [2], biological applications [3] and heterogeneous photocatalysis [4]. These materials can be obtained as a heterostructure, heterojunction or core/shell, and has been explored for allowing versatility of properties and applications. It is known that in recent years several studies have explored the modification of semiconductors by means of substitutional or interstitial doping creating short-range distortions in the crystalline lattice, vacancies of anions or cations, energy sub-levels and thus influencing various properties of the materials [5]. However research in this field gained a new dimension to explore the changes in the properties by interfacial interactions in which fascinating discoveries have been made. In this sense, we can mention the metallic behavior between interfaces of the insulating perovskites [6]; or the multiferroic behavior presented by stress of interface [7], better photocatalytic and sensing properties when compared to separated materials [8,9], and an improvement of photocatalytic behavior caused by coupling of $SrTiO_3$ on the TiO_2 nanosheets [10].

Among the several new researches about heterojunctions, the interface between the TiO_2 and the $SrTiO_3$ materials has been interesting to us, since they are presented as materials of different structures, with close values of band gap, and with flat band potential of the $SrTiO_3$ slightly higher than that of TiO_2 [11]. TiO_2 crystallizes commonly in the tetragonal phase rutile, although by changes in thermal processing the TiO_2 also stabilizes in tetragonal anatase phase. This phase presents advantages for being photoactive phase with band gap around 3.2 eV and unit cell parameters $a = 3.78$ Å, and, $c = 9.51$ Å. On the other hand, $SrTiO_3$ presents perovskite cubic unit cell with lattice parameter $a = b = c = 3.90$ Å, and a semiconductor band gap value similar to TiO_2 anatase phase (3.2 eV) [12]. In $SrTiO_3$ structure the Sr^{2+} and O^{2-} ions form the cubic lattice with the Ti^{4+} ions occupying the octahedral spaces created by the oxygens [13]. From the several existing works we

---

[*] Corresponding author.
E-mail addresses: rafaelciola@yahoo.com.br, rafaelciola@hotmail.com (R.A.C. Amoresi).

http://dx.doi.org/10.1016/j.jeurceramsoc.2017.10.056
Received 22 August 2017; Received in revised form 26 October 2017; Accepted 29 October 2017

observed that the mechanisms of obtaining for the heterojunction TiO_2/$SrTiO_3$ refers in the growth of $SrTiO_3$ on the structures of TiO_2 [10,11], however, we did not find the reverse. This is important from the point of view about interfaces and microstructural, to alterations of the electronic and optical properties as a function of interfacial energy difference [14].

Our research group has evaluated the optical and electronic properties of several titanates perovskites ($ATiO_3$, where A = Ca, Sr, Ba) through photoluminescence emission behaviors [15–17], which optical properties of these materials is related to charge transfer between octahedral clusters [TiO_6] and [$TiO_5.V_o^y$] and between polyhedral clusters [AO_{12}] and [$AO_{11}.V_o^y$]. The emission phenomenon is attributed to localized energy states above the valence band (VB) and below conduction band (BC), which is directly related to degree of order-disorder on clusters. However, these works are related to single phase materials and not for heterojunctions with interface formed with different chemical compounds, phases and crystalline lattices tensions. It has been reported in several works that physical chemistry parameters deriving from growth surface between materials [18] and from synthesis procedure [19,20] can promote changes in crystalline phase stability, and hence changes on energy emission behavior. Different synthesis have been proposed in order to modulate the heterostructure properties, but, traditional methods are generally complex [10,14,21,22]. In this work, we present a new and facile synthesis route of $SrTiO_3/TiO_2$ nanocomposite material with highly dispersed particles presented.

The objectives of our work were to present the novel synthesis method, but also discuss the formation of the interface between $SrTiO_3$/TiO_2 with crystallization of titanium dioxide on the cubic crystal system of $SrTiO_3$. This allows us to show the difference between pure and heterojunctions materials obtained for two different $SrTiO_3$ concentration related to TiO_2, being these 1% and 5% wt. Structural evaluation for order-disorder in materials were discussed by long and short range order. We infer from these, the effects of crystalline lattice tension and changes in local symmetry. Then, we showed the effect of local structural distortion with $SrTiO_3$ content on photoluminescence emission. Ultimately, we showed the crystalline lattice stress by transmission electronic microscopy related to crystal growth on interface of $SrTiO_3/TiO_2$.

2. Experimental section

To preparation the sol-gel solution of Ti, titanium (IV) isopropoxide (97%, Aldrich) was mixed with glacial acetic acid (99.7% Qhemis) in molar ratio of 1:4, under constant stirring to form the complex. Thereafter, isopropyl alcohol (99.5%, Vetec) was added to the solution, which remained under stirring for 1 h. To preparation of stable suspension and samples, initially the $SrTiO_3$ particles were prepared via polymeric precursor method (PPM), as previously described [23]. For obtainment route of $SrTiO_3/TiO_2$ heterojunction was divided into two steps. In the first step was done the hydroxylation of $SrTiO_3$ particles surface by addition of H_2O_2 (20–60%, Vetec), NH_4OH (28–30%, Qhemis), in the deionized water to particles dispersion, which has stirred for 30 min at 50 °C. After the solution cooling at room temperature it was added drops of acrylic acid (99%, Aldrich), 2-methoxyethanol (99.8%, Aldrich), polyvinyl alcohol (PVA) (99.6%, Vetec), and isopropanol to obtain a $SrTiO_3$ stable suspension. The second step is the formation of $SrTiO_3$-TiO_2 core-shell system that was prepared by addition of $SrTiO_3$ stable suspension into sol-gel solution of Ti. Then, the resulting mixture remained at room temperature under stirring for 24 h to promote the coating of $SrTiO_3$ particles by TiO_2 gel. Then, the components are called TST-1% and TST-5% heterojunctions, to 1% and 5%, respectively, in the mass of $SrTiO_3$ particles added into the sol-gel solution of Ti. To obtain pure TiO_2, was used the same procedure. The materials were dried at 100 °C for 24 h, and heat treatment was done at 500 °C for 4 h in the muffle furnace.

The structural analyzes of samples were carried out by X Ray diffraction (XRD) on a diffractometer Rigaku, Model Rint 2000. The crystallite size of samples it was estimated by Scherrer's formula. The Raman spectroscopy characterization was done by LabRAM iHR550 Horiba Jobin Yvon spectrometer with a laser of wavelength of 514 nm, as an excitation source, and spectral resolution of 1 cm^{-1}, with 40 scans, in the range 100–800 cm^{-1}. The particle morphology was investigated by field emission scanning electron microscopy (FE-SEM) on a JEOL FEG-SEM model 7500F, and high resolution transmission electron microscopy by transmission electron microscopy (TEM-FEI/PHILIPS CM120). Physical adsorption of nitrogen at low temperatures (77 K) was used to measure the surface area by the Brunauer-Emmett-Teller method in a Micrometrics ASAP 2010 equipment and Barrett-Joyner-Halenda (BJH) method to calculate the pores volume. The photonic characteristics were analyzed by UV–vis diffuse reflectance using a Perkin Elmer UV/Vis/NIR Lambda 1050 spectrophotometer. Besides that, the photoluminescence spectra were collected through a Thermo Jarrell Ash 27 cms monochromator with a Hamamatsu photomultiplier model R955 using a krypton laser Coherent Innova 200 with wavelength output at 350 nm as an excitation source.

3. Results and discussion

3.1. $SrTiO_3$ colloidal stability

The new route to obtain $SrTiO_3/TiO_2$ heterojunction with homogeneous distribution throughout the sample was developed and allowed the formation of a solid-solid interface. The novel route of synthesis was based on the formation of a stable colloidal suspension of $SrTiO_3$ particles, which was added to a titanium sol-gel solution. The high stability of suspension has based on two mains principles, electrostatic and steric. The electrostatic influence was achieved by the $SrTiO_3$ particles surface modification using hydroxylation processes by H_2O_2, which increase the stability and reactivity by the adsorption of OH groups on its surface. The pH value of the suspension was then adjusted to 9 with NH_4OH, which facilitates the release of H^+, instead the complete OH, from the groups adsorbed on the particle surface by the effect of the high concentration of OH^- in solution. Thus, H^+ from surface binds with an OH^- from PVA, releasing a H_2O molecule and the remained $SrTiO_3—O^-$ binds with the remained C^+ from PVA, generating and $SrTiO_3—O—R$ bond, being R the carbon chain of the PVA molecule without the hydroxyl, by covalent bonding. As a consequence, PVA molecules covering the particles generate the steric contribution, which are the lines covering the $SrTiO_3$ particles, that is responsible for avoiding the agglomeration of particles on suspension due to the steric repulsion forces between the polymer chains [24,25].

In order to enhance the colloidal stability of $SrTiO_3$ dispersion also, 2-methoxyethanol and isopropanol were added, they have low dielectric constant, 17.41 for 2-methoxyethanol [26] and 18.62 for isopropanol, in contrast to 80.37 for water (all at 20 °C) [27]. Therefore, these organic solvents increase the charge density of the electric double layer of particles, increasing the zeta potential [26]. Since $SrTiO_3$ is a n-type semiconductor, negative surface charge arises from its nature and also by the hydroxylation process, hence the Stern layer has composed by counter ions in relation to the surface charge, resulting in a greater amount of positive charges (+) around these particles. According to Helmholtz-Smoluchowski theory, the smaller the dielectric constant of a liquid medium, higher is the zeta potential of a dispersed particle, allowing then higher colloidal stability [28]. This route avoid the agglomeration of particles and promotes homogeneous distribution of $SrTiO_3$ on the titanium sol-gel, based on electrostatic-steric stabilization, ensuring the coating of these particles by the formation of $SrTiO_3$/TiO_2 heterojunction on the synthesis route.

3.2. Field emission scanning electron microscopy (FE-SEM)

Fig. 1 shows the micrographs and histograms of particle size

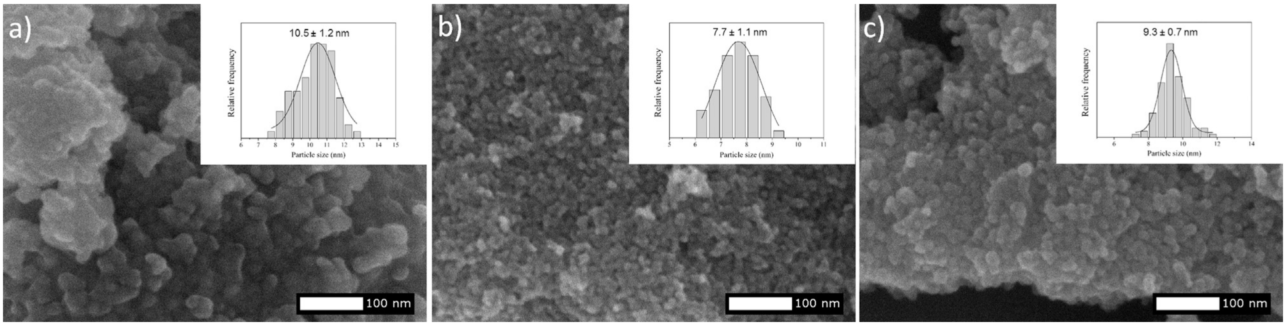

Fig. 1. FE-SEM images and histograms (inset) of pure TiO_2 (a), TST-1% (b) and TST-5% (c).

Table 1
Microstructural characteristics of pure TiO_2, TST-1% and TST-5% samples.

Sample	Average particle size (nm)	Pore volume ($cm^3\ g^{-1}$)	Specific surface area ($m^2\ g^{-1}$)	Average anatase crystallite size (nm)
TiO_2	10.5 ± 1.2	0.136	72.0	13.1
TST-1%	7.7 ± 1.1	0.261	165.5	9.4
TST-5%	9.3 ± 0.7	0.374	139.8	12.4

distribution in inset of pure TiO_2, TST-1% and TST-5% samples. The pure TiO_2, Fig. 1a, it resulted in an average particle size of 10.5 nm, spherical and dispersed, as was to be expected since the morphology and particle agglomeration are strongly dependent on the concentration and composition of organic solvent in the synthesis [29]. The nanocomposite TST-1% and TST-5%, Fig. 1b and c, respectively, it also observed the spherical particles with an average size of 8 nm and 9 nm, respectively. As can be seen in Table 1, the high specific surface area of the samples may be related to the use of the organic additives. The introduction of highly dispersed particles, in the process of heterojunction formation, increase in the average space between agglomerates of particles, which was observed in larger volumes of pores, more dispersed particles, and the significant increase in specific surface area of nanocomposite samples compared to pure TiO_2, it is important for catalytic and optical properties because improve the contact area and increases the probability of surface defects.

3.3. X-ray diffraction (XRD)

X-ray diffraction was employed to investigate the crystalline phase as well the structural properties at long-range order. As shown in Fig. 2 XRD patterns of $SrTiO_3$, pure TiO_2 and $SrTiO_3/TiO_2$ heterojunction, indicate to the $SrTiO_3$ only polycristalline cubic phase is observed, from the space group Pm-3 m (ICSD – n° 23076). For the pure TiO_2, only tetragonal anatase phase is evident, space group I41/amd (ICSD – n° 9852). The existence of pure TiO_2 anatase phase is in agreement with its thermodynamic stability at the applied treatment temperature (500 °C) [30]. For TST-1% only TiO_2 anatase phase was detected because of the content of $SrTiO_3$ is lower than limit of detection. For the TST-5% heterojunction the anatase TiO_2 and the $SrTiO_3$ cubic phases were observed. A widening reflection peaks of TiO_2 anatase phase it was observed for both heterojunction samples, which reflects a decrease in the sizes of anatase crystallites as showed in Table 1. No displacement of TiO_2 anatase phase peaks is observed in the heterojunction indicating that no reaction occurred between $SrTiO_3$ and TiO_2, i.e. there was no solid solution formation. This leads to indications that the interactions between both materials are only by solid-solid interface formation.

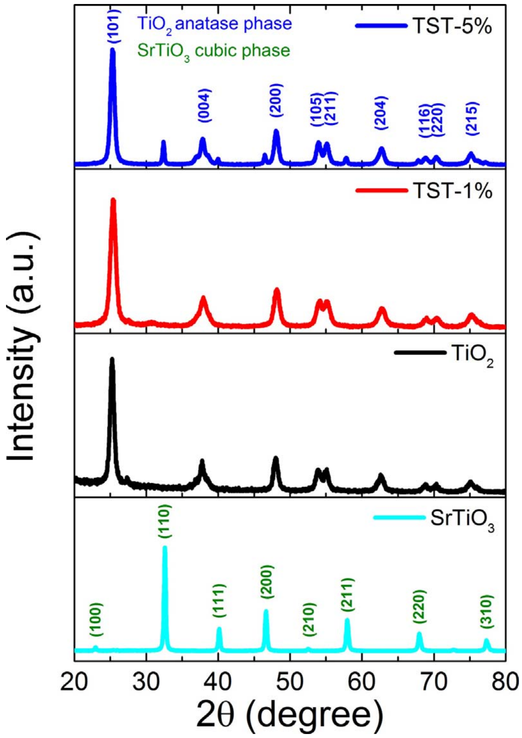

Fig. 2. XRD patterns employed to investigate the crystalline phase and the structural properties at long-range order of $SrTiO_3$, pure TiO_2, TST-1% and TST-5% samples.

3.4. Micro-Raman scattering spectroscopy

Fig. 3 shows the micro-Raman spectra of pure TiO_2 and $SrTiO_3/TiO_2$ heterojunction. For all samples, the Raman shifts bands observed is characteristic of vibrational modes related to symmetries of TiO_2 anatase structure, which supports XRD results. There are six Raman active optical modes in this phase, which are A_{1g}, $2B_{1g}$ and $3E_g$. These Raman shifts are located at approximately at 144 cm^{-1} ($E_{g(1)}$), 197 cm^{-1} ($E_{g(2)}$), 399 cm^{-1} ($B_{1g(1)}$), 513 cm^{-1} (A_{1g}), 519 cm^{-1} ($B_{1g(2)}$) and 639 cm^{-1} ($E_{g(3)}$) [31]. A typical broad band was observed at 513–519 cm^{-1}, which is characteristic of an overlap in the values of Raman shifts of A_{1g} and B_{1g} vibrational modes. No Raman shifts related to vibrational modes of $SrTiO_3$ structure were detected, this because such system crystallize in the cubic perovskite structure which has a high degree of symmetry, resulting no representative signal. For the heterojunction TST-1% a displacement of the peak $E_{g(1)}$ is observed for the region of higher energy, as shown in Fig. 3b, and for TST-5% heterojunction, besides the displacement it was observed a suppression of the $B_{1g(1)}$, A_{1g}, $B_{1g(2)}$, $E_{g(3)}$ bands.

Several factors contribute to peak displacement, or band widening for Eg mode in the TiO_2, such as phonon confinement, particle size heterogeneity, defects, nonstoichiometry and stress of lattice [32,33]. In our results we found no line broadening in mode $E_{g(1)}$ for any sample, since the size and distribution of the particle are homogeneous as seen in Fig. 1. However in the case of a heterojunction is expected in the

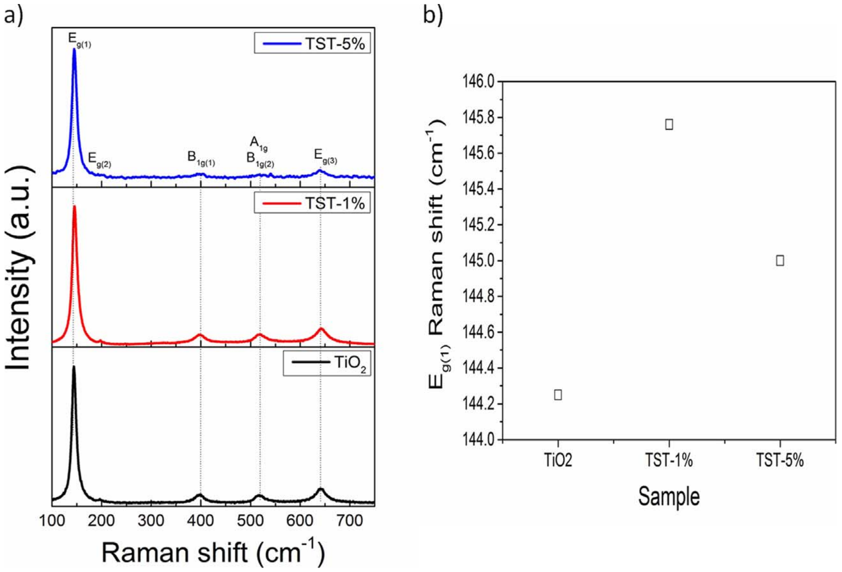

Fig. 3. Raman spectra in the range from 100 cm^{-1} to 800 cm^{-1} for of a) pure TiO_2, TST-1% and TST-5% samples, and (b) displacement of the center of the peak $E_{g(1)}$ for the samples.

region of the interface between the cubic perovskite $SrTiO_3$ and the growth of the TiO_2 tetragonal phase that there are effects of stress and defects in such region. Tension and compression stress affect the Raman lines through shifts to red and blue, respectively [34,35]. When we refer to the cristalization of tetragonal anatase TiO_2 on a cubic structure of $SrTiO_3$, a compression stress on the crystalline lattice of binary oxide is clearly expected.

In addition to structural stress, short-range defects are also present, as observed in changes of the $E_{g(1)}$ band, which is the most intense Raman shift peak of TiO_2 anatase structure. This vibrational mode has assigned to the O—Ti—O bond-bending mode in [TiO_6] octahedrons [36]. Thus the blue-shift of peak $E_{g(1)}$ also can associate to the formation of a linkage of two [TiO_6] octahedrons at the interface region of heterojunction. This linkage results in O_T—Ti_T—$O_{T/S}$ bonds, in which T represents the octahedron of TiO_2 and T/S is the shared oxygen with the both kinds of distorted octahedrons, one from tetragonal TiO_2 and other form cubic $SrTiO_3$, on the interface region [37]. Since TiO_2 tetragonal and interface region presents different crystal systems, the coordination parameters of octahedrons are different. This feature confers a variation in $E_{g(1)}$ vibrational mode of TiO_2 anatase phase and consequently a slight blue shift of this peak [38]. Therefore, the formation of an interface on $SrTiO_3/TiO_2$ heterojunction leads to disorder at short-range of TiO_2 anatase phase, and the degree of these distortions of [TiO_6] clusters increases with increasing $SrTiO_3$ amount. As observed in Fig. 3, Raman spectrum of TST-5% sample shows a decrease in the intensities of Raman shifts bands related to all vibrational modes of TiO_2 anatase structure. The high degree of distortion on [TiO_6] clusters leads to a break of local symmetry, and hence a restraint of vibrational modes, thus decreasing the intensities of bands related to these modes.

3.5. *UV–vis diffuse reflectance spectroscopy*

Fig. 4 shows the UV–vis absorption spectra and Tauc plot of $SrTiO_3$, pure TiO_2, TST-1%, and TST-5% samples. The absorption spectra were plot from correlation between diffuse reflectance data and its absorbance by Kubelka-Munk algorithm [39]. As can be seen in Fig. 4a, all samples presents higher absorbance in wavelength shorter than 400 nm, which results from electron transitions of valence band to conduction band, and these absorbance decreases as the photon energy is lower than the band gap energy of each material. Fig. 4b shows the Tauc plot for determining the band gap energy of all samples by the intercept in abscissas axis of a linear fit of the $(\alpha h\nu)^{1/2}$ vs. $h\nu$ plots, where α is the absorbance and $h\nu$ the photon energy, considering indirect band gap for TiO_2 anatase and $SrTiO_3$ cubic [40,41]. Table 2 shows the optical band gap energies and photon wavelength edge for absorption of all prepared samples. The band gap energies of pure TiO_2 and $SrTiO_3$ were lower than literature data [42,43], which is related to method and conditions of synthesis which confers intrinsic defects resulting in a reduction of band gap energy [44]. For TST-1% and TST-5% samples, two regions of exponential decays were observed, which is characteristic of a heterostructured material due to the existence of at least two phases in the material. Both heterojunctions samples exhibited band gap energies lower than the each separated material, which are attributed to the presence of structural order-disorder in materials caused by defects on interface [45], indicating electronic transitions between bands of both structures. More remarkable in TST-1% sample, with has lowest band gap energy, confirming the synergistic effect in bands structure of phases.

3.6. *Photoluminescence (PL)*

In order to explore the electronic transitions and investigate the nature of defects within all materials, PL measurements were performed at room temperature. As shown in Fig. 5, the pure TiO_2 presents emission center at 550 nm, green region, with the highest emission intensity of photoluminescence compared to other materials. The $SrTiO_3$ among all the materials has the lowest emission intensity and its center is in the violet region at 445 nm. However, both heterojunctions shows PL intensity higher than pure $SrTiO_3$, which indicates that the mechanism of light emission is mainly by TiO_2 structure and confirming the formation of heterojunction. This is in agreement with well-known mechanism of electron transfer on $SrTiO_3/TiO_2$ heterostructure, since electronic bands of $SrTiO_3$ has lower reduction potential than the TiO_2 [41,46,47]. Therefore, excited electrons on $SrTiO_3$ tend to migrate to TiO_2 structure, recombining in this and hence emitting photons. Furthermore, both heterojunctions presents PL intensity lower than that of pure TiO_2, indicating that the recombination rate of the electron-hole pairs was decreased. This reduction on PL intensities is related to the formation of electronic states density within the band gap due to order-disorder effects, which is clearly observed in Raman analysis. These structural distortions on [TiO_6] provides a high density of energies states that might contribute to non-radiative emission due to low energy difference between these levels, thus reducing the contribution of radioactive emission and hence the PL signal [48].

For further understanding about PL emission, all spectra were analyzed by deconvolution of bands with Gauss and Voigt G/L

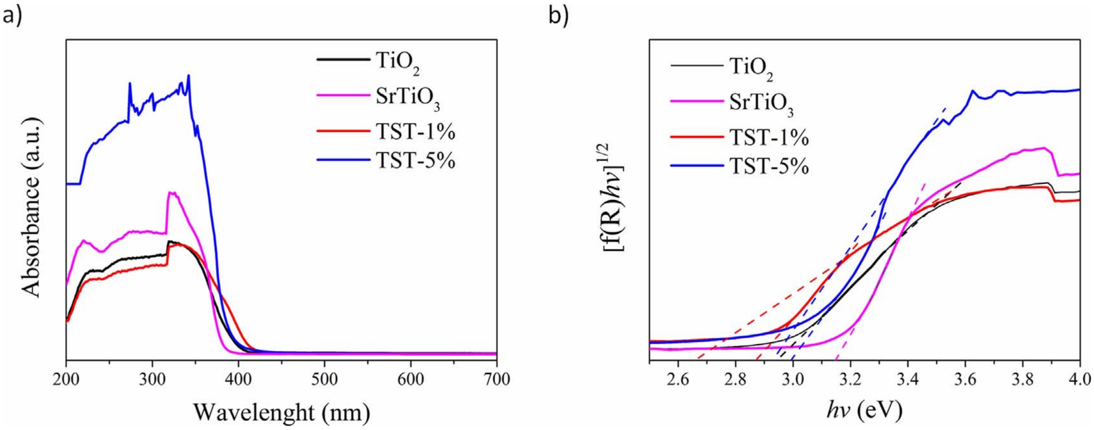

Fig. 4. (a) UV–vis spectra and (b) Tauc plot of pure TiO_2, $SrTiO_3$, TST-1% and TST-5% samples.

Table 2
Energies and photon wavelengths edge of band gap of pure TiO_2, TST-1%, TST-5%, and $SrTiO_3$ samples.

Sample	TiO_2	TST-1%	TST-5%	$SrTiO_3$
E_g (eV)	2.94 (R^2: 0.998)	2.87 (R^2: 0.997) 2.66 (R^2: 0.996)	2.99 (R^2: 0.997) 2.93 (R^2: 0.998)	3.15 (R^2: 0.999)
λ_{gap} (nm)	422	466	423	394

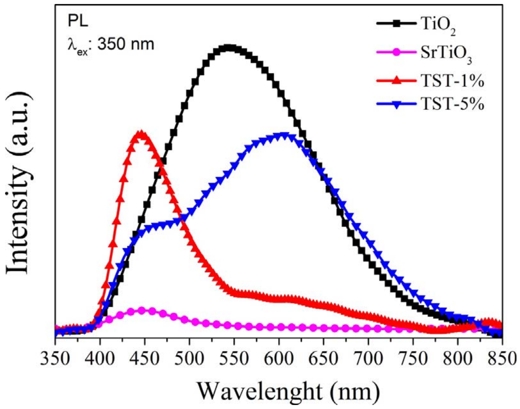

Fig. 5. Spectrum of PL emission at room temperature under an air atmosphere for pure TiO_2, $SrTiO_3$, and heterojunctions TST-1% and TST-5% samples.

functions. For pure TiO_2, the PL emission has a typical broad band characteristic of multiphonon processes, i.e. emission occurs by several paths due to high density of electronic states within the band gap, allowing the relaxation of electron before the radiative recombination [15,49]. This band has maximum emission intensity centered at approximately 550 nm, which is well-known characteristic of TiO_2 anatase structure [17,50,51]. The defects presents in this structure responsible for emission in large range of visible spectrum are mainly related to oxygen vacancy [50–52], being these considered to be $V_o^{\bullet}$ and $V_o^{\bullet\bullet}$, which are single and double ionized oxygen vacancy, respectively. Thus, generated clusters has the form [$TiO_5.V_o^{\bullet}$] and [$TiO_5.V_o^{\bullet\bullet}$]. For anatase phase of TiO_2, it has been reported by calculations that $V_o^{\bullet\bullet}$ is the most stable oxygen vacancy at normal conditions, while $V_o^{\bullet}$ is unstable due to the unpaired electron [53]. Therefore, the energy level of $V_o^{\bullet}$ is higher than $V_o^{\bullet\bullet}$, which is explainable by its stability. Furthermore, it has been reported that these oxygen vacancies occupy positions of energy levels up to 1.18 eV below the conduction band minimum on TiO_2 anatase structure [54,55]. According to experimental data obtained for optical band gap energies of the samples, a mechanism was proposed for explain the changes in their PL behaviors. The deconvolution results of PL spectrum of pure TiO_2 are shown in Fig. 6a and b, which indicates contributions of green and yellow region of visible spectrum. The energies of the photons with the emitted wavelengths were calculated through Eq. (1), which comes from Planck-Einstein relation, which E is the photon energy in eV and λ the photon wavelength in nm.

$$E = \frac{1240}{\lambda} \tag{1}$$

The mechanism proposed for PL emission of pure TiO_2 is shown in Fig. 7a, which indicates the excitation of electrons from valence band to conduction band, and then, both kinds of oxygen vacancies act as trapping sites for these electrons on their decay. Once these electrons are trapped in these defects, their recombination to valence band emits photons with wavelengths, and hence colors, characteristics to observed spectrum. Since optical band gap energy of pure TiO_2 was obtained as 2.94 eV, the energies levels of oxygen vacancies in this sample were considered to be 0.49 eV and 0.83 eV below the conduction band minimum, according to emitted photon energy. The green emission exhibited by pure TiO_2 is related to electron trapping by $V_o^{\bullet}$ and yellow emission to electron trapping by $V_o^{\bullet\bullet}$, since the position of $V_o^{\bullet\bullet}$ energy level of $V_o^{\bullet}$ is higher and closer to conduction band minimum than

Therefore, the green emission band of pure TiO_2 has its center composed by photons with 2.45 eV and the yellow emission band by photons with 2.11 eV of energies. The mostly emission in yellow region for pure TiO_2 anatase phase, which arising from contributions of $V_o^{\bullet\bullet}$ defects is clearly expected, since it is the most stable oxygen vacancy for this structure in normal conditions [53]. However, a smaller contribution of $V_o^{\bullet}$ defects for PL emission was also observed due to order-disorder effects resulting from synthesis conditions.

Fig. 6c and d shows the deconvolution results of PL spectrum of $SrTiO_3$. According to $SrTiO_3$ structure has a cubic crystal system and high symmetry, it would not be expected to presents PL emission, since this phenomenon arises from structural disorder effects [56,57]. Although, this is not what was observed in these results. As reported in literature, PL emission of $SrTiO_3$ is due to the presence of intermediate energy levels within the band gap formed by structural distortions on clusters and oxygen vacancies [15,16,57], which can easily trap electrons and holes, respectively, inducing PL emission in visible spectrum. Longo et al. reported the synthesis and photoluminescence properties of $SrTiO_3$ with center emission band in the green region, thus indicating that the positions of energy levels of these defects within band gap is dependent of degree of structural order-disorder [58]. Despite the PL emission of our experimental results for $SrTiO_3$, its PL intensity is low compared to other materials, which is clearly expected due to higher symmetry of $SrTiO_3$ perovskite crystal system. Therefore, PL measurements is a powerful measurement detecting medium-range disorder in

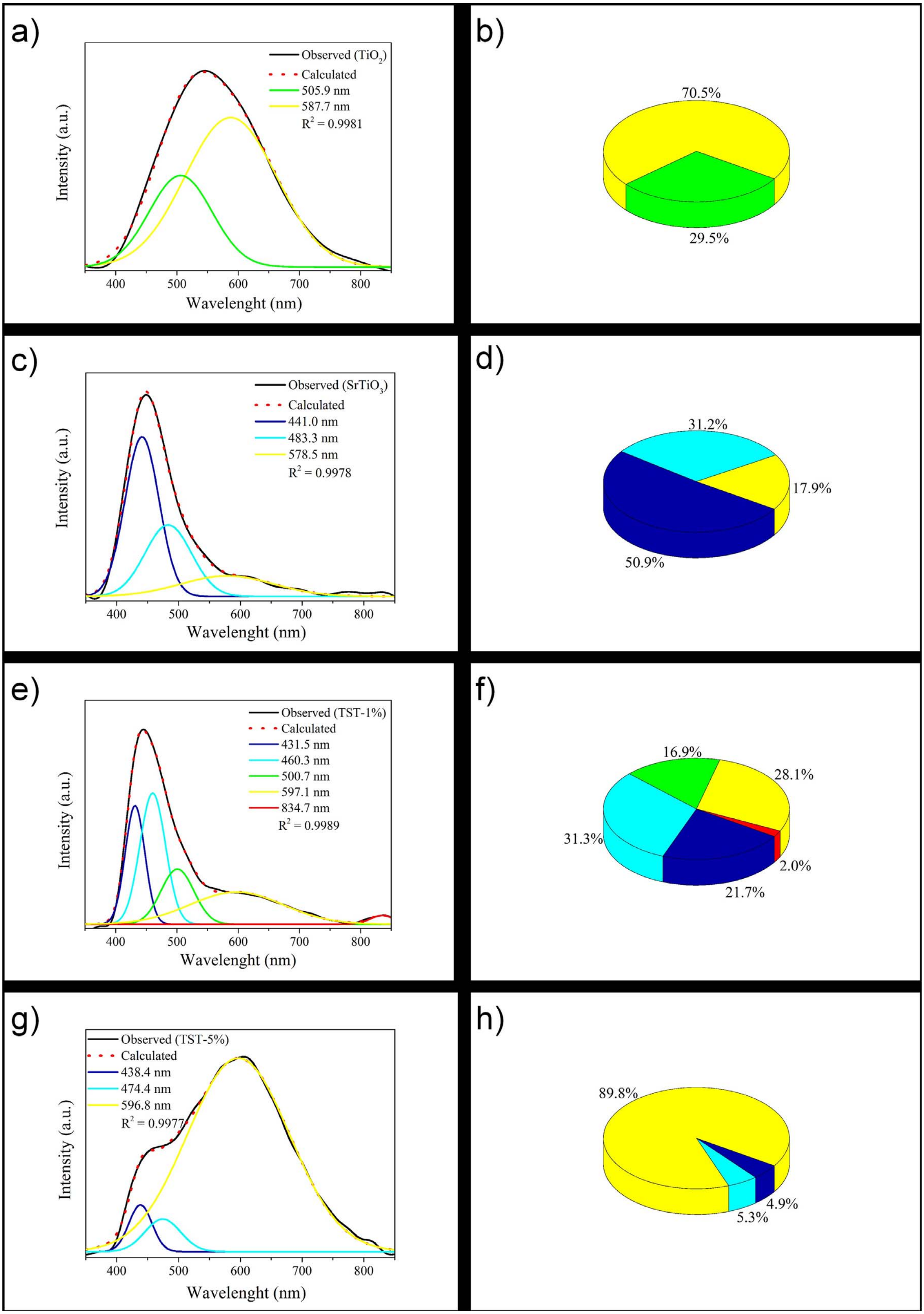

Fig. 6. Deconvolution of the spectra PL and percentage of each area deconvoluted for samples a–b) TiO_2 pure, c–d) $SrTiO_3$, e–f) heterojunção TST-1%, and g–h) heterojunção TST-5%.

$SrTiO_3$ structure, which it was not possible by XRD and Raman analysis [59].

Fig. 6e and f shows the deconvolution results of PL spectrum of TST-1% sample. As discussed earlier, $SrTiO_3$ has a low PL emission intensity, thus PL emission of both heterojunctions arises mainly from TiO_2 structure, confirming the charge transfer at the interface and heterojunction formation. It is clearly observed in the spectrum a significant band shift for higher emission energy and a narrowing of the band.

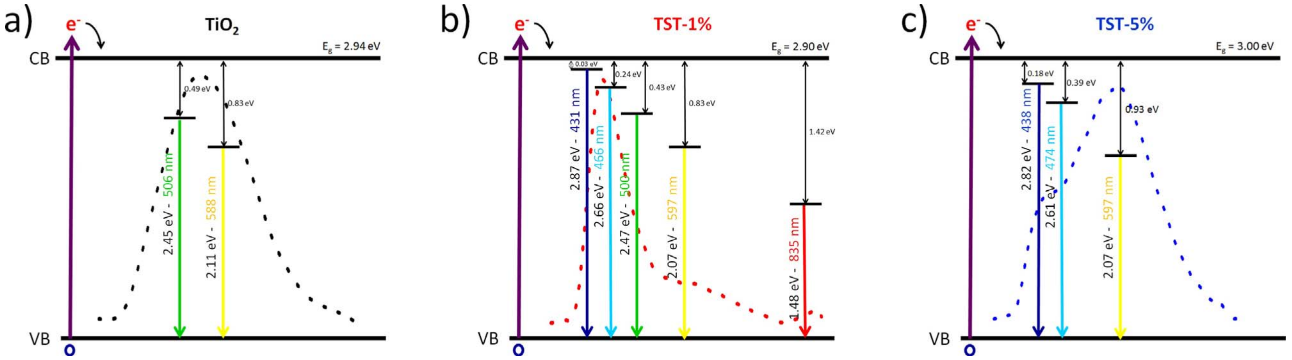

Fig. 7. Scheme of energy decay of the PL for the sample a) TiO_2, b) TST-1%, and c) TST-5%.

Since the blue and green PL emission in TiO_2 anatase structure was associated to energy levels formed by $V_o^{\bullet}$ defects, a remarkable contribution of this defect for emission must be expected. According to short-range properties of heterojunctions samples obtained by Raman analysis, distortions in $[TiO_6]$ clusters was observed, which arises from formation of a $SrTiO_3/TiO_2$ interface. These observed distortions comes from changes in coordination parameters of $[TiO_6]$ clusters, i.e. bonds lengths and angles, since $E_{g(1)}$ mode of TiO_2 anatase structure is due to bond bending of O—Ti—O bonds, as discussed in Raman analysis. These structural distortions of clusters can induce the promotion of stable vacancy $V_o^{\bullet\bullet}$ for unstable vacancy $V_o^{\bullet}$, since the concept of oxygen vacancy in TiO_2 is believed to be changes in bond lengths Ti–O, i.e. how far the oxygen is from titanium and how many electrons still participate in this interaction [17]. Hereupon, an excess of $V_o^{\bullet}$ defects is responsible for 69.9% of PL emission of TST-1%, and a contribution of 28.1% by $V_o^{\bullet\bullet}$ is presents as observed in yellow emission. An interesting feature observed for TST-1% sample is an emission in near-infrared with 2.0% of contribution for total spectrum. This contribution is the well-known emission originated of defects in TiO_2 rutile phase, centered at approximately 835 nm [60–62]. Although in structural analyzes were not possible to detect TiO_2 rutile phase, PL measurements is very sensitive to detect electronic defects in materials [59]. Fig. 7b shows the mechanism proposed for TST-1% PL emission.

Fig. 6g and h shows the deconvolution results of PL spectrum of TST-5% sample. It is clearly observed in this spectrum a large broadening and band shift for lower energy compared to TST-1% PL spectrum. According to Raman analysis of heterojunctions samples, increasing amount of $SrTiO_3$ induces more structural disorder of $[TiO_6]$ clusters, as observed in reduced bands intensities of inelastic scattering due to freedom quenching of vibrational modes for TST-5%. Therefore, an increase in blue and green emission it would be expected for TST-5% PL spectrum. However, a significant increase in yellow emission it was observed, which suggests an increase in $V_o^{\bullet\bullet}$ concentration defects in TiO_2 anatase structure. The significant increase in structural distortions of $[TiO_6]$ clusters observed from TST-1% to TST-5% favored the conversion from $V_o^{\bullet}$ to $V_o^{\bullet\bullet}$ defects due to increase in $SrTiO_3$ content. In order to maintain the charge equilibrium into lattice, this phenomenon of vacancy charge conversion occurs since for charge compensation, one $V_o^{\bullet\bullet}$ equals to two $V_o^{\bullet}$ defects. Therefore, the increase in $SrTiO_3$ amount stabilizes $V_o^{\bullet\bullet}$ since a very high amount of $V_o^{\bullet}$ it would be necessary. A broad PL band was observed for TST-5% sample, indicating a high density of energy states within band gap which induces the multiphonon processes. As observed in deconvolution results, yellow emission is responsible for 89.8% of total spectrum and 10.2% of blue emission, confirming the mainly contribution of $V_o^{\bullet\bullet}$ defects. Fig. 7c shows the mechanism proposed for PL emission of TST-5% sample. Therefore, PL results allowed exploring the kinds of structural defects generated depending on degree of order-disorder caused by formation of $SrTiO_3/TiO_2$ interface, and allows us to infer that in a heterojunction not always the increase of one of the components will represent the increase in a specific emission. The modulation of the properties involve qualitative contributions of the defects and tensions. Based on that we use TEM analyzes to explore the characteristics of the tensions at the interface.

3.7. High resolution transmission electron microscopy (HR-TEM)

HR-TEM analyzes were performed in order to further elucidate the tensions present on interfaces, the crystalline structure and morphology of the particles. Fig. 8a shows that the TST-5% presents spherical and

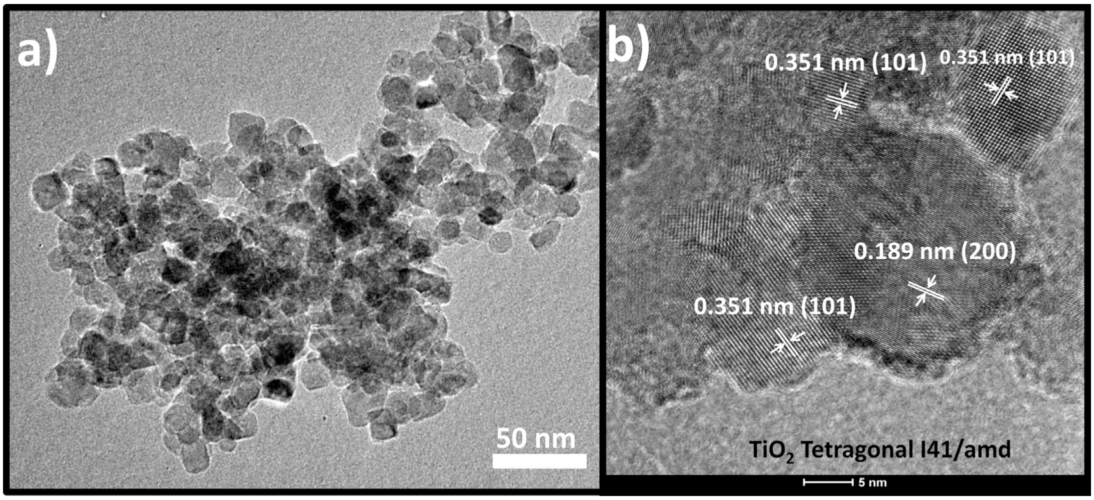

Fig. 8. TEM and HRTEM images for the T-ST5% sample. a) TEM of the T-ST5% particles, b) HRTEM of a region of polycrystalline TiO_2 grains.

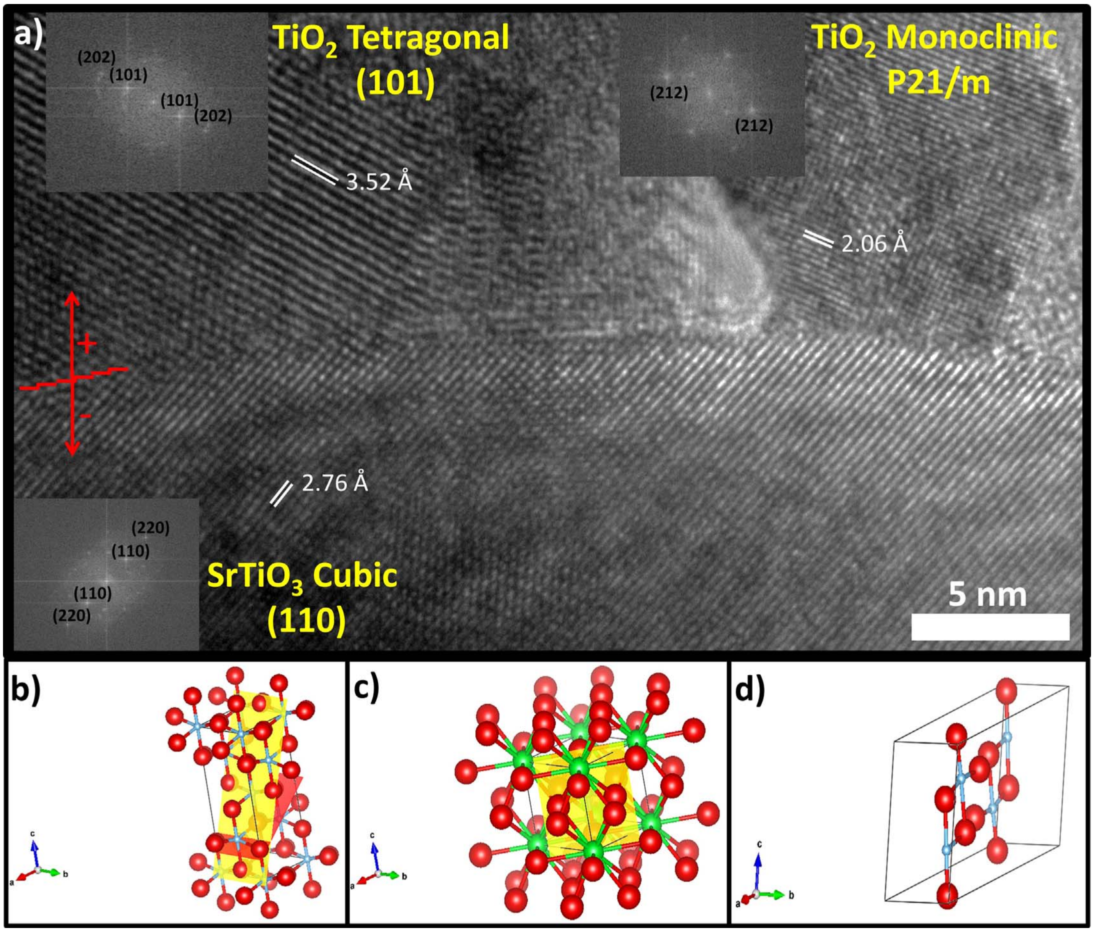

Fig. 9. a) HRTEM images for the $SrTiO_3/TiO_2$ interface region. The insets are referents the Fourier transform (FFT) pattern for each region of the image and the corresponding crystalline structures, for the structure of the b) tetragonal TiO_2 in yellow corresponds to the plane (101) and in red for the plane (103), c) $SrTiO_3$ cubic for the (110) plane and d) monoclinic TiO_2 phase. (For interpretation of the references to color in this figure legend, the reader is referred to the web version of this article.)

cubic particles with size around 12 nm to 20 nm. Fig. 8b shows the high resolution TEM image for a region where there are isolated TiO_2 particles which were identified anatase crystalline phase, corroborating with XRD results. Fig. 9 shows an interface region in which TiO_2 crystallizes on the $SrTiO_3$ particles, as verified by the crystal lattice spacing to both $SrTiO_3$ and TiO_2.

Fig. 9a shows the calculated distances of 3.52 Å and 2.76 Å, which are in well agreement with d-spacing (101) plane of anatase tetragonal TiO_2 (Fig. 9b – $a = b \neq c$ and $\alpha = \beta = \gamma = 90°$) and of (110) plane of cubic phase of $SrTiO_3$ (Fig. 9c), respectively. In addition, it was verified a metastable phase not identified by XRD and Raman analysis correspondent to a region with d-spacing 2.06 Å, which we infer to the plane (212) of monoclinic TiO_2 phase (Fig. 9d, space group *P21/m* – $a \neq b \neq c$ and $\alpha = \gamma = 90° \neq \beta$). This metastable phase is confined only to a medium range region in the interfaces. For each region of the image are shown its corresponding Fast Fourier transform (FFT) patterns (insets in Fig. 9a), that confirm the calculated spacing. Based on these results, it was possible to verify the presence of two interfaces. One interface has formed between $SrTiO_3$ cubic/anatase tetragonal TiO_2 phase and the other one exists on the $SrTiO_3$ cubic/monoclinic TiO_2 phase, in order to simplify we designate the interfaces by $STO_C/TiO_{2\text{-}A}$ and $STO_C/TiO_{2\text{-}M}$, respectively. The growth of the tetragonal anatase TiO_2 ($a = 3.784$ Å) on the cubic $SrTiO_3$ ($a = 3.905$ Å) is plausible because the mismatch is only -3.1%, also the monoclinic phase, considering the parameter b (3.741 Å), possible presents similar interface stress.

Structural distortions in interface region were analyzed as shown in Fig. 10. As can be observed in graph, the zero point on the abscissa corresponds to the region of interface between the grains of $SrTiO_3$ and the crystalline planes of TiO_2, represented in Fig. 9 by a horizontal red line. The negative values for this axis correspond to the direction of the interface towards the middle of the grain of $SrTiO_3$, and the positive values correspond to the direction of the interface towards the crystallization of the planes of TiO_2. The axis of the ordinates of the graph of Fig. 10 corresponds to the interplanar distances calculated for each region, being in this method for each calculated distance five d-spacing analyzes were done to ensure that the sub-pixel characterization leads to a precision of structural evolution. It is possible to observe the variations depending on the distance of the interface in relation to the d-spacing, similar to the peak-pair analysis [63]. The dotted lines corresponds to the d-spacing of the $SrTiO_3$ and TiO_2 planes according to the database (ICSD n°: 23076; n°: 9852; n°: 657748).

It was found that for all planes near interface there are changes of the d-spacing in relation to theoretical values. Based on the fact that the coefficient of thermal expansion of TiO_2 [64] and of $SrTiO_3$ [65] are different, both will be under stress during the heat treatment. Resulting after cooling in changes in the interplanar spacing of the crystalline lattice, mainly near the interface region. We observed that the grain of $SrTiO_3$ when presenting a compression stress region (Fig. 10a) has compensated by another region with an expansion stress (Fig. 10b). In this case, the stress of compression of the crystalline lattice favors the crystallization of the tetragonal anatase phase of TiO_2, resulting in the $STO_C/TiO_{2\text{-}A}$ interface, and the expansion stress allows crystallization of the monoclinic TiO_2 phase, resulting in the $STO_C/TiO_{2\text{-}M}$. At the $STO_C/TiO_{2\text{-}A}$ interface, the growth of the TiO_2 anatase tetragonal phase on $SrTiO_3$ cubic also occurs by tensions in the lattice of TiO_2. As was

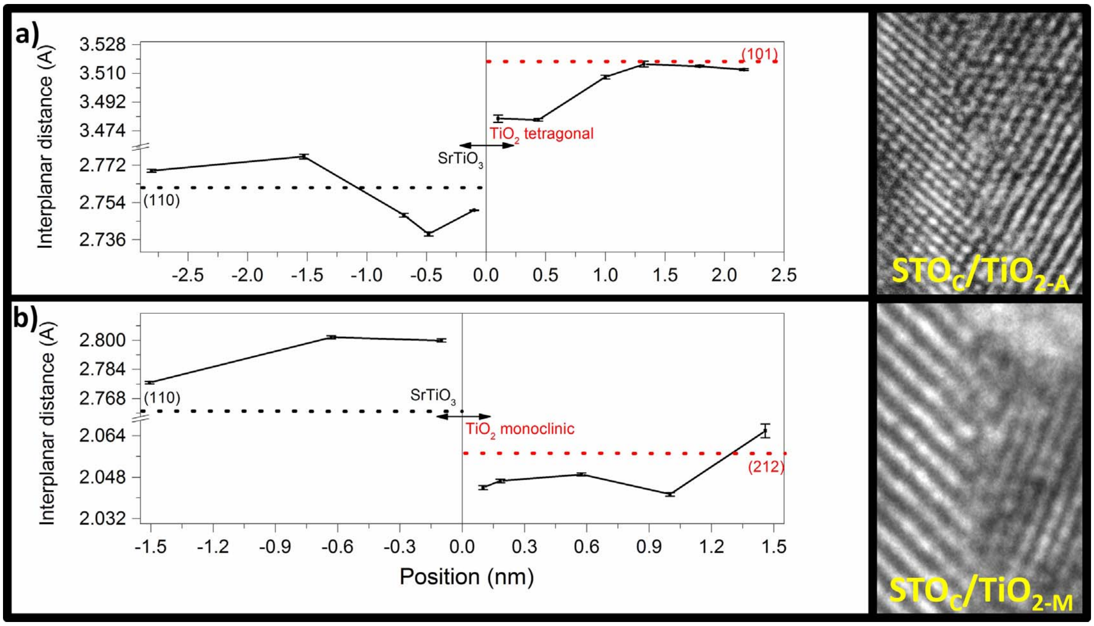

Fig. 10. a) Structural distortions in interface region analyzed by d-spacing calculated between a) $STO_C/TiO_{2\text{-}A}$ and b) $STO_C/TiO_{2\text{-}M}$ regions. The dotted lines correspond to the d-spacing of the $SrTiO_3$ and TiO_2 planes according to theoretical values.

studied by Oropeza et al. [18] which showed that the interface region of TiO_2 is composed by facets {103} that have higher energy and lower angle compared to facets {101}, and in addition, the faceted plane {103} of TiO_2 has similar surface energy ($1.05\ J\ m^{-2}$) relative to the surface energy of (110) planes of $SrTiO_3$, $1.01\ J\ m^{-2}$ [66], and this favors the growth of this phase. These facets are show as planes in Fig. 9b, the yellow color corresponds to the (101) plane and red for the (103) plane.

The growth of the TiO_2 monoclinic phase in estimated (212) plane occurs under a region where there is an expansion of the interplanar distance (110) of $SrTiO_3$ to 2.80 Å, as shown in Fig. 10b. Since the monoclinic phase comes from the original lattice type of a distorted cubic system [67] it is supported the growth of this phase on the interface with the $SrTiO_3$ cubic phase. Several works [19,20,68] reported the phase transitions between different levels of symmetry (cubic, tetragonal and monoclinic), and emphasize that among the factors for the transition are the temperature increase in the interface that entails in entropy variation, serving as the driving force for the transition of phase. Goutenoire et al. [69] evaluating the transition from monoclinic to cubic phase in the $La_2Mo_2O_9$ system, reported that the higher symmetry is obtained by oxygen diffusion in the crystalline lattice according to the temperature variation. Thus, we believe that the surface of the $SrTiO_3$ cubic of high symmetry allows the transition in the interface to the monoclinic phase of TiO_2 due to factors such as the increase of surface entropy with the synthesis temperature and diffusion of oxygen atoms between octahedral clusters $[TiO_6]$ and polyhedral $[SrO_{12}]$. This results in an interfacial stress between clusters as verified in Raman spectroscopy analyzes, and favors the formation of the monoclinic phase. Therefore, as already discussed, the variation of defects on clusters and oxygen vacancies at the interface as observed in the Raman spectra, photoluminescence spectra and TEM analyzes generates important information of interface stresses and defects generated in the structure in heterojunctions.

4. Conclusion

$SrTiO_3/TiO_2$ heterojunctions were successfully prepared by association of sol-gel method with stable colloidal suspension of $SrTiO_3$ particles. This simple and inexpensive route allowed the formation of a solid-solid interface responsible for modifications on electronic and optical properties, due to the improvement in charge carrier transfer in this region. This procedure does not use controlled atmosphere, high pressure or high temperature, avoiding high agglomeration and promoting homogeneous particles distribution based on electrostatic-steric stabilization, being an important factor for optical and catalytic applications of materials. XRD, Raman and diffuse reflectance analyzes indicated structural order-disorder at long and short range. PL results allowed exploring the kinds of structural defects generated depending on degree of order-disorder on lattice. Furthermore, the linkage of structural and PL analyzes allowed a better understanding of interface effects on optical properties of $SrTiO_3/TiO_2$ heterojunctions. Increasing $SrTiO_3$ concentration on heterojunctions caused an increase in structural disorder due to structural mismatch on interface of $SrTiO_3/TiO_2$, which led to different types of defects, since significant proportion of $V_o^{\bullet}$ converted to $V_o^{\bullet\bullet}$, altering abruptly PL emission properties of these materials. Therefore, PL behavior of heterojunctions was not directly related to percentage composition of both phases due to their characteristics emissions, but strongly dependent of the kinds and concentration of structural defects generated by interface phenomena. Hereupon, this allows modulating desirable properties for heterojunctions materials to applications such as led or selective colors emitters, altering its color emission by controlling materials phase proportions and hence structural defects. TEM analyzes showed how the different thermal expansion of the grain influence the stress caused in the interface region, either by expansion stress or compression stress, resulting in the growth of intermediate phases, corroborating Raman and photoluminescence results on the tensions and defects present in the heterojunctions. Therefore, the understanding of interface effects gives rises to perspectives for potentials future applications of heterojunctions materials.

Acknowledgments

The authors would like to warmly express their gratitude and indebtedness to the São Paulo Research Foundation (FAPESP) (Grant CEPID/CDMF – FAPESP: 2013/07296-2) and the National Council for Scientific and Technological Development (CNPq) for the financial support granted in the course of this research. We are also grateful to the LMA-IQ for providing the FEG-SEM facilities.

References

[1] J. Ren, W. Que, X. Yin, Y. He, H.M.A. Javed, Novel fabrication of TiO_2/ZnO nanotube array heterojunction for dye-sensitized solar cells, RSC Adv. 4 (2014) 7454, http://dx.doi.org/10.1039/c3ra45741a.

[2] L.I. Trakhtenberg, G.N. Gerasimov, V.F. Gromov, T.V. Belysheva, O.J. Ilegbusi, Gas semiconducting sensors based on metal oxide nanocomposites, J. Mater. Sci. Res. 1 (2012) 56–68, http://dx.doi.org/10.5539/jmsr.v1n2p56.

[3] M.A. Khan, A. Ahmad, K. Umar, S.A. Nabi, Synthesis, characterization, and biological applications of nanocomposites for the removal of heavy metals and dyes, Ind. Eng. Chem. Res. 54 (2015) 76–82, http://dx.doi.org/10.1021/ie504148k.

[4] L. Wang, Z. Wang, D. Wang, X. Shi, H. Song, X. Gao, The photocatalysis and mechanism of new $SrTiO_3$/TiO_2, Solid State Sci. 31 (2014) 85–90, http://dx.doi.org/10.1016/j.solidstatesciences.2014.03.005.

[5] M.S. Silva, R.G. Dias, E.F. Souza, M. Cilense, M.A. Zaghete, A.A. Cavalheiro, Effect of strontium doping on the structural, morphological, and dielectric properties of PZT ceramics, Mater. Sci. Forum 869 (2016) 8–12, http://dx.doi.org/10.4028/www.scientific.net/MSF.869.8.

[6] A. Ohtomo, H.Y. Hwang, A high-mobility electron gas at the $LaAlO_3$/$SrTiO_3$ heterointerface, Nature 427 (2004) 423–426, http://dx.doi.org/10.1038/nature02308.

[7] P.P. Ortega, L.S.R. Rocha, C.C. Silva, M. Cilense, R.A.C. Amoresi, E. Longo, A.Z. Simões, Multiferroic behavior of heterostructures composed of lanthanum and bismuth ferrite, Ceram. Int. 42 (2016) 16521–16528, http://dx.doi.org/10.1016/j.ceramint.2016.07.070.

[8] S. Rajendran, M.M. Khan, F. Gracia, J. Qin, V.K. Gupta, S. Arumainathan, Ce^{3+}-ion-induced visible-light photocatalytic degradation and electrochemical activity of ZnO/CeO_2 nanocomposite, Sci. Rep. 6 (2016) 31641, http://dx.doi.org/10.1038/srep31641.

[9] L. Huo, X. Yang, Z. Liu, X. Tian, T. Qi, X. Wang, K. Yu, J. Sun, M. Fan, Modulation of potential barrier heights in Co_3O_4/SnO_2 heterojunctions for highly H_2-selective sensors, Sens. Actuators B Chem. 244 (2017) 694–700, http://dx.doi.org/10.1016/j.snb.2017.01.061.

[10] X. Yue, J. Zhang, F. Yan, X. Wang, F. Huang, A situ hydrothermal synthesis of $SrTiO_3$/TiO_2 heterostructure nanosheets with exposed (001) facets for enhancing photocatalytic degradation activity, Appl. Surf. Sci. 319 (2014) 68–74, http://dx.doi.org/10.1016/j.apsusc.2014.07.100.

[11] X. Zhang, K. Huo, L. Hu, Z. Wu, P.K. Chu, Synthesis and photocatalytic activity of highly ordered TiO_2 and $SrTiO_3$/TiO_2 nanotube arrays on Ti substrates, J. Am. Ceram. Soc. 93 (2010) 2771–2778, http://dx.doi.org/10.1111/j.1551-2916.2010.03805.x.

[12] F. Lenzmann, J. Krueger, S. Burnside, M. Grtzel, D. Gal, S. Rhle, D. Cahen, K. Brooks, M. Gra, S. Ru, Surface photovoltage spectroscopy of dye-sensitized solar cells with TiO, NbO, and SrTiO nanocrystalline photoanodes: indication for electron injection from higher excited dye states $SrTiO_3$, J. Phys. Chem. B (2001) 6347–6352, http://dx.doi.org/10.1021/jp010380q.

[13] M. Johnsson, P. Lemmens, Crystallography and chemistry of perovskites, Handb. Magn. Adv. Magn. Mater. (2007) 1–11, http://dx.doi.org/10.1002/9780470022184.hmm411.

[14] S. Chen, T. Cao, Y. Gao, D. Li, F. Xiong, W. Huang, Probing surface structures of CeO_2, TiO_2, and Cu_2O nanocrystals with CO and CO_2 chemisorption, J. Phys. Chem. C 120 (2016) 21472–21485, http://dx.doi.org/10.1021/acs.jpcc.6b06158.

[15] V.M. Longo, A.T. De Figueiredo, S. De Lázaro, M.F. Gurgel, M.G.S. Costa, C.O. Paiva-Santos, J.A. Varela, E. Longo, V.R. Mastelaro, F.S. De Vicente, A.C. Hernandes, R.W.A. Franco, Structural conditions that leads to photoluminescence emission in $SrTiO_3$: an experimental and theoretical approach, J. Appl. Phys. 104 (2008), http://dx.doi.org/10.1063/1.2956741.

[16] A.E. Souza, G.T.A. Santos, B.C. Barra, W.D. Macedo, S.R. Teixeira, C.M. Santos, A.M.O.R. Senos, L. Amaral, E. Longo, Photoluminescence of $SrTiO_3$: influence of particle size and morphology, Cryst. Growth Des. 12 (2012) 5671–5679, http://dx.doi.org/10.1021/cg301168k.

[17] E. Silva Jr., F.A. La Porta, M.S. Liu, J. Andrés, J.A. Varela, E. Longo, A relationship between structural and electronic order–disorder effects and optical properties in crystalline TiO_2 nanomaterials, Dalt. Trans. 44 (2015) 3159–3175, http://dx.doi.org/10.1039/c4dt03254c.

[18] F.E. Oropeza, K.H.L. Zhang, A. Regoutz, V.K. Lazarov, D. Wermeille, C.G. Poll, R.G. Egdell, Growth of epitaxial anatase nano islands on $SrTiO_3$ (001) by dip coating, Cryst. Growth Des. 3 (2013).

[19] S. Bevara, K.K. Mishra, S.J. Patwe, T.R. Ravindran, M.K. Gupta, R. Mittal, P.S.R. Krishna, A.K. Sinha, S.N. Achary, A.K. Tyagi, Phase transformation, vibrational and electronic properties of $K_2Ce(PO_4)_2$: a combined experimental and theoretical study, Inorg. Chem. 56 (2017) 3335–3348, http://dx.doi.org/10.1021/acs.inorgchem.6b02870.

[20] B. Shatschneider, J.-J. Liang, S. Jerowski, A. Tkachenko, Phase transition between cubic and monoclinic polymorphs of tetracyanoethylene crystal: the role of temperature and kinetics bohdan schatschneider, Cryst. Eng. Comm. 14 (2012) 4656–466.

[21] H. Huang, D. Li, Q. Lin, W. Zhang, Y. Shao, Y. Chen, M. Sun, X. Fu, Efficient degradation of benzene over $LaVO_4$/TiO_2 nanocrystalline heterojunction photocatalyst under visible light irradiation, Environ. Sci. Technol. 43 (2009) 4164–4168, http://dx.doi.org/10.1021/es900393h.

[22] D. Guerrero-Araque, D. Ramírez-Ortega, P. Acevedo-Peña, F. Tzompantzi, H.A. Calderón, R. Gómez, Interfacial charge-transfer process across ZrO_2-TiO_2 heterojunction and its impact on photocatalytic activity, J. Photochem. Photobiol. A Chem. 335 (2017) 276–286, http://dx.doi.org/10.1016/j.jphotochem.2016.11.030.

[23] G. Gasparotto, G.F. Teixeira, M.A. Cebim, J.A. Varela, L.A. Perazolli, M.A. Zaghete, Influence of the preparation route on the structural, morphological and spectroscopic properties of $SrTiO_3$ and $SrTiO_3$:Eu^{3+} powders, MRS Online Proce. Library Arch. 1507 (2013) 1–6.

[24] A.J. Worthen, V. Tran, K.A. Cornell, T.M. Truskett, K.P. Johnston, Steric stabilization of nanoparticles with grafted low molecular weight ligands in highly concentrated brines including divalent ions, Soft Matter 12 (2016) 2025–2039, http://dx.doi.org/10.1039/C5SM02787J.

[25] S. Elbasuney, Sustainable steric stabilization of colloidal titania nanoparticles, Appl. Surf. Sci. 409 (2017) 438–447, http://dx.doi.org/10.1016/j.apsusc.2017.03.013.

[26] C.M. Kinart, W.J. Kinart, D. Szychowski, Dielectric properties of binary mixtures of dipropylene glycol monomethyl ether with 2-methoxyethanol and water at various temperatures, Phys. Chem. Liq. 43 (2005) 103–109, http://dx.doi.org/10.1080/00319100512331328701.

[27] G. Akerlof, Dielectric constants of some organic solvent-water mixtures at various temperatures, J. Am. Chem. Soc. 54 (1932) 4125–4139, http://dx.doi.org/10.1021/ja01350a001.

[28] S. Bhattacharjee, DLS and zeta potential – what they are and what they are not? J. Control. Release 235 (2016) 337–351, http://dx.doi.org/10.1016/j.jconrel.2016.06.017.

[29] B. Moongraksathum, D.S. Lee, Y.W. Chen, Monodispersibility and size control in the preparation of spherical titania particles by thermal hydrolysis of $TiCl_4$ in various solvents, J. Taiwan Inst. Chem. Eng. 68 (2016) 455–460, http://dx.doi.org/10.1016/j.jtice.2016.09.010.

[30] G. Li, L. Li, J. Boerio-Goates, B.F. Woodfield, High purity anatase TiO_2 nanocrystals: near room-temperature synthesis, grain growth kinetics, and surface hydration chemistry, J. Am. Chem. Soc. 127 (2005) 8659–8666, http://dx.doi.org/10.1021/ja050517g.

[31] T. Ohsaka, F. Izumi, Y. Fujiki, Raman spectrum of anatase, TiO_2, J. Raman Spectrosc. 7 (1978) 321–324, http://dx.doi.org/10.1002/jrs.1250070606.

[32] A. Golubovic, M. Scepanovic, A. Kremenovic, S. Askrabic, V. Berec, Z. DohCevic-Mitrovic, Z.V. Popovic, Raman study of the variation in anatase structure of TiO_2 nanopowders due to the changes of sol-gel synthesis conditions, J. Sol-Gel Sci. Technol. 49 (2009) 311–319, http://dx.doi.org/10.1007/s10971-008-1872-3.

[33] I.H. Campbell, P.M. Fauchet, The effects of microcrystal size and shape on the one phonon Raman spectra of crystalline semiconductors, Solid State Commun. 58 (1986) 739–741, http://dx.doi.org/10.1016/0038-1098(86)90513-2.

[34] F. Cerdeira, C.J. Buchenauer, F.H. Pollak, M. Cardona, Stress-induced Raman shifts of diamond and zincblende semiconductor, Phys. Rev. B 5 (1972) 580, http://dx.doi.org/10.1103/PhysRevB.5.580.

[35] M. Šćepanović, M. Grujić-Brojčin, Z. Dohčević-Mitrović, Z.V. Popović, Effects of confinement, strain and nonstoichiometry on raman spectra of anatase TiO_2, nanopowders, Mater. Sci. Forum 518 (2006) 101–106, http://dx.doi.org/10.4028/www.scientific.net/MSF.518.101.

[36] J.C. Parker, R.W. Siegel, Raman microprobe study of nanophase TiO_2 and oxidation-induced spectral changes, J. Mater. Res. 5 (1990) 1246–1252, http://dx.doi.org/10.1557/JMR.1990.1246.

[37] Y.-J. Du, Z.H. Li, K.-N. Fan, Periodic density functional theory studies of the VO_x/TiO_2 (anatase) catalysts: structure and stability of monomeric species, Surf. Sci. 606 (2012) 956–964, http://dx.doi.org/10.1016/j.susc.2012.02.016.

[38] J. Tao, Z. Gong, G. Yao, Y. Cheng, M. Zhang, J. Lv, S. Shi, G. He, X. Jiang, X. Chen, Z. Sun, Enhanced optical and photocatalytic properties of Ag quantum dots-sensitized nanostructured TiO_2/ZnO heterojunctions, J. Alloys Compd. 688 (2016) 605–612, http://dx.doi.org/10.1016/j.jallcom.2016.07.074.

[39] B.J. Wood, Diffuse reflectance spectra and optical properties of some sulphides and related minerals, Miner. Mag. 43 (1979) 509–518, http://dx.doi.org/10.1180/minmag.1979.043.328.11.

[40] K. Van Benthem, C. Elsässer, R.H. French, Bulk electronic structure of $SrTiO_3$: experiment and theory, J. Appl. Phys. 90 (2001) 6156–6164, http://dx.doi.org/10.1063/1.1415766.

[41] M.N. Ha, F. Zhu, Z. Liu, L. Wang, L. Liu, G. Lu, Z. Zhao, Morphology-controlled synthesis of $SrTiO_3$/TiO_2 heterostructures and their photocatalytic performance for water splitting, RSC Adv. 6 (2016) 21111–21118, http://dx.doi.org/10.1039/C6RA03472A.

[42] C. Wang, H. Qiu, T. Inoue, Q. Yao, Band gap engineering of $SrTiO_3$ for water splitting under visible light irradiation, Int. J. Hydrogen Energy 39 (2014) 12507–12514, http://dx.doi.org/10.1016/j.ijhydene.2014.06.059.

[43] V. Etacheri, C. Di Valentin, J. Schneider, D. Bahnemann, S.C. Pillai, Visible-light activation of TiO_2 photocatalysts: advances in theory and experiments, J. Photochem. Photobiol. C Photochem. Rev. 25 (2015) 1–29, http://dx.doi.org/10.1016/j.jphotochemrev.2015.08.003.

[44] B. Choudhury, S. Bayan, A. Choudhury, P. Chakraborty, Narrowing of band gap and effective charge carrier separation in oxygen deficient TiO_2 nanotubes with improved visible light photocatalytic activity, J. Colloid Interface Sci. 465 (2016) 1–10, http://dx.doi.org/10.1016/j.jcis.2015.11.050.

[45] R.A. Roca, J.C. Sczancoski, I.C. Nogueira, M.T. Fabbro, H.C. Alves, L. Gracia, L.P.S. Santos, C.P. de Sousa, J. Andrés, G.E. Luz, E. Longo, L.S. Cavalcante, Facet-dependent photocatalytic and antibacterial properties of α-Ag_2WO_4 crystals: combining experimental data and theoretical insights, Catal. Sci. Technol. 5 (2015) 4091–4107, http://dx.doi.org/10.1039/C5CY00331H.

[46] E. Guo, L. Yin, Tailored $SrTiO_3$/TiO_2 heterostructures for dye-sensitized solar cells with enhanced photoelectric conversion performance, J. Mater. Chem. A 3 (2015) 13390–13401, http://dx.doi.org/10.1039/C5TA02556G.

[47] Z. Wu, Y. Su, J. Yu, W. Xiao, L. Sun, C. Lin, Enhanced photoelectrocatalytic hydrogen production activity of $SrTiO_3$-TiO_2 hetero-nanoparticle modified TiO_2

nanotube arrays, Int. J. Hydrogen Energy 40 (2015) 9704–9712, http://dx.doi.org/10.1016/j.ijhydene.2015.06.036.

[48] T. Chevallier, A. Benayad, G. Le Blevennec, F. Chandezon, Method to determine radiative and non-radiative defects applied to $AgInS_2$-ZnS luminescent nanocrystals, J. Phys. Chem. Chem. Phys. 19 (2017) 2359–2363, http://dx.doi.org/10.1039/C6CP06509K.

[49] M.L. Moreira, M.F.C. Gurgel, G.P. Mambrini, E.R. Leite, P.S. Pizani, J.A. Varela, E. Longo, Photoluminescence of barium titanate and barium zirconate in multilayer disordered thin films at room temperature, J. Phys. Chem. A 112 (2008) 8938–8942, http://dx.doi.org/10.1021/jp801610y.

[50] J. Shi, J. Chen, Z. Feng, T. Chen, Y. Lian, X. Wang, C. Li, Photoluminescence characteristics of TiO_2 and their relationship to the photoassisted reaction of water/methanol mixture, J. Phys. Chem. C 111 (2007) 693–699, http://dx.doi.org/10.1021/jp065744z.

[51] X. Wang, Z. Feng, J. Shi, G. Jia, S. Shen, J. Zhou, C. Li, Trap states and carrier dynamics of TiO2 studied by photoluminescence spectroscopy under weak excitation condition, Phys. Chem. Chem. Phys. 12 (2010) 7083–7090, http://dx.doi.org/10.1039/b925277k.

[52] M. Vishwas, K.N. Rao, R.P.S. Chakradhar, Influence of annealing temperature on Raman and photoluminescence spectra of electron beam evaporated TiO_2 thin films, Spectrochim. Acta Part A Mol. Biomol. Spectrosc. 99 (2012) 33–36, http://dx.doi.org/10.1016/j.saa.2012.09.009.

[53] H. Li, Y. Guo, J. Robertson, Calculation of TiO_2 surface and subsurface oxygen vacancy by the screened exchange functional, J. Phys. Chem. C 119 (2015) 18160–18166, http://dx.doi.org/10.1021/acs.jpcc.5b02430.

[54] N. Zhang, Y. Xu, Defective TiO_2 with oxygen vacancies: synthesis, properties and photocatalytic applications, Nanoscale 5 (2013) 3601–3614, http://dx.doi.org/10.1039/c3nr00476g.

[55] N. Serpone, D. Lawless, R. Khairutdinov, Size effects on the photophysical properties of colloidal anatase TiO_2 particles: size quantization versus direct transitions in this indirect semiconductor? J. Phys. Chem. 99 (1995) 16646–16654, http://dx.doi.org/10.1021/j100045a026.

[56] M.L. Moreira, M.F.C. Gurgel, G.P. Mambrini, E.R. Leite, P.S. Pizani, J.A. Yarda, E. Longo, Photoluminescence of barium titanate and barium zirconate in multilayer disordered thin films at room temperature, J. Phys. Chem. A 112 (2008) 8938–8942, http://dx.doi.org/10.1021/jp801610y.

[57] L. Gracia, J. Andrés, V.M. Longo, J.A. Varela, E. Longo, A theoretical study on the photoluminescence of $SrTiO_3$, Chem. Phys. Lett. 493 (2010) 141–146, http://dx.doi.org/10.1016/j.cplett.2010.05.041.

[58] V.M. Longo, L.S. Cavalcante, M.G.S. Costa, M.L. Moreira, A.T. de Figueiredo, J. Andrés, J.A. Varela, E. Longo, First principles calculations on the origin of violet-blue and green light photoluminescence emission in $SrZrO_3$ and $SrTiO_3$ perovskites, Theor. Chem. Acc. 124 (2009) 385–394, http://dx.doi.org/10.1007/s00214-009-0628-7.

[59] L.S. Cavalcante, J.C. Sczancoski, L.F. Lima, J.W.M. Espinosa, P.S. Pizani, J.A. Varela, E. Longo, Synthesis, characterization, anisotropic growth and photoluminescence of $BaWO_4$, Cryst. Growth Des. 9 (2009) 1002–1012, http://dx.doi.org/10.1021/cg800817x.

[60] X. Wang, S. Shen, Z. Feng, C. Li, Time-resolved photoluminescence of anatase/rutile TiO_2 phase junction revealing charge separation dynamics, Cuihua Xuebao/Chin. J. Catal. 37 (2016) 2059–2068, http://dx.doi.org/10.1016/S1872-2067(16)62574-3.

[61] D.K. Pallotti, L. Passoni, P. Maddalena, F. Di Fonzo, S. Lettieri, Photoluminescence mechanisms in anatase and rutile TiO_2, J. Phys. Chem. C 121 (2017) 9011–9021, http://dx.doi.org/10.1021/acs.jpcc.7b00321.

[62] L. Kernazhitsky, V. Shymanovska, T. Gavrilko, V. Naumov, L. Fedorenko, V. Kshnyakin, J. Baran, Room temperature photoluminescence of anatase and rutile TiO_2 powders, J. Lumin. 146 (2014) 199–204, http://dx.doi.org/10.1016/j.jlumin.2013.09.068.

[63] P.L. Galindo, High resolution peak measurement and strain mapping using peak pairs analysis, Microsc. Anal. 23 (2009) 23–25.

[64] L. Iyengar, Thermal Expansion of Rutile and Anatase, (1969), pp. 1969–1971.

[65] D. De Ligny, P. Richet, High-temperature heat capacity and thermal expansion of $SrTiO_3$ and $SrZrO_3$ perovskites, Phys. Rev. B Condens. Matter. 53 (1996) 3013–3022.

[66] T. Sano, D.M. Saylor, G.S. Rohrer, Surface energy anisotropy of $SrTiO_3$at 1400 °C in air, J. Am. Ceram. Soc. 86 (2003) 1933–1939.

[67] R. Marchand, L. Brohan, M. Tournoux, TiO_2(B) a new form of titanium dioxide and the potassium octatitanate $K_2Ti_8O_{17}$, Mater. Res. Bull. 15 (1980) 1129–1133, http://dx.doi.org/10.1016/0025-5408(80)90076-8.

[68] L. Malavasi, H. Kim, S.J.L. Billinge, T. Proffen, C. Tealdi, G. Flor, Nature of the monoclinic to cubic phase transition in the fast oxygen ion conductor $La_2Mo_2O_9$ (LAMOX), J. Am. Chem. Soc. 9 (2007) 6903–6907.

[69] F. Goutenoire, O. Isnard, R. Retoux, P. Lacorre, Crystal structure of $La_2Mo_2O_9$, a new fast oxide- ino conductor, Chem. Mater. (2014) 2575–2580.